9324 *J. Phys. Chem. A* **2008,** *112,* 9324–9335

Correlated Angular and Quantum State-Resolved CO_2 Scattering Dynamics at the Gas−Liquid Interface[†]

Bradford G. Perkins, Jr. and David J. Nesbitt*

JILA, University of Colorado and National Institute of Standards and Technology, and Department of Chemistry and Biochemistry, University of Colorado, Boulder, Colorado 80309-0440

Received: March 16, 2008; Revised Manuscript Received: June 18, 2008

Molecular beam scattering dynamics at the gas−liquid interface are investigated for CO_2 ($E_{inc} = 10.6(8)$ kcal/mol) impinging on liquid perfluoropolyether (PFPE), with quantum state (υ, J) populations measured as a function of incident (θ_{inc}) and final (θ_{scat}) scattering angles. The internal state distributions are well-characterized for both normal and grazing incident angles by a two-component Boltzmann model for trapping desorption (TD) and impulsive scattering (IS) at rotational temperatures T_{rot}(TD/IS), where the fractional TD probability for CO_2 on the perfluorinated surface is denoted by TD and IS densities (ρ) as $\alpha = \rho_{TD}/(\rho_{TD} + \rho_{IS})$. On the basis of an assumed $\cos(\theta_{scat})$ scattering behavior for the TD flux component, the angular dependence of the IS flux at normal incidence ($\theta_{inc} = 0°$) is surprisingly well-modeled by a simple $\cos^n(\theta_{scat})$ distribution with $n = 1.0 \pm 0.2$, while glancing incident angles ($\theta_{inc} = 30°$, 45°, and 60°) result in lobular angular IS distributions scattered preferentially in the forward direction. This trend is also corroborated in the TD fraction α, which decreases rapidly under non-normal incident conditions as a function of backward versus forward scattering direction. Furthermore, the extent of rotational excitation in the IS channel increases dramatically with increasing angle of incidence, consistent with an increasing rotational torque due to surface roughness at the gas−liquid interface.

I. Introduction

The study of both reactive and inelastic collisions in the gas phase represents an enormously fertile area of research interest, toward which Professor Stephen R. Leone has made seminal contributions over the last several decades.[1−9] As a result of such pioneering efforts by Leone and others in the chemical physics community, our understanding of state-to-state gas-phase collision dynamics has reached new heights of predictive power, control, and elegance.[3,10−15] An equivalent intellectual framework for understanding state-to-state collision dynamics at the gas−liquid interface has proven more elusive, toward which recent efforts in our group have been dedicated.[16−21] The desire for greater understanding of such interfacial dynamics is motivated by both practical and fundamental interests. Indeed, gas−condensed-phase interactions arguably play a major role in a wide range of chemical phenomena such as industrial synthesis,[22] combustion,[23] aerosols,[24,25] pollution,[26] atmospheric ozone depletion,[27−29] as well as many other heterogeneous chemical processes.

For a gas molecule to dissolve, for example, it must first collide with the surface, at which point it may either directly scatter back into the gas or become temporarily trapped long enough to lose memory of its initial collision conditions. If trapped, the gas can simply desorb or proceed along a complicated path where it could diffuse across the interface or finally dissolve into the liquid before reappearing some time later. To help understand such interfacial dynamics, elegant molecular beam time-of-flight mass spectrometry (TOFMS) experiments[30−34] and theoretical molecular dynamics simulations[35−42] have been developed to explore the physical and chemical properties that impact molecular trajectory dynamics at the gas−liquid surface. From these studies and many others, the gas−liquid scattering event has been usefully characterized primarily by the two scattering pathways illustrated in Figure 1, though, more accurately, a continuum of such channels must clearly exist. These pathways have been simply indentified as (i) "trapping desorption" (TD) events, where all memory of the incident collision is lost through interactions that range from direct collisions, physisorption, and momentary solvation, and (ii) "impulsive scattering" (IS) events, which entail limited gas−liquid collisions that potentially sample nonequilibrium dynamical processes. In both experimental and theoretical studies, the TD versus IS nature of these two channels has been identified by final kinetic energy analysis.[43,44] For molecular

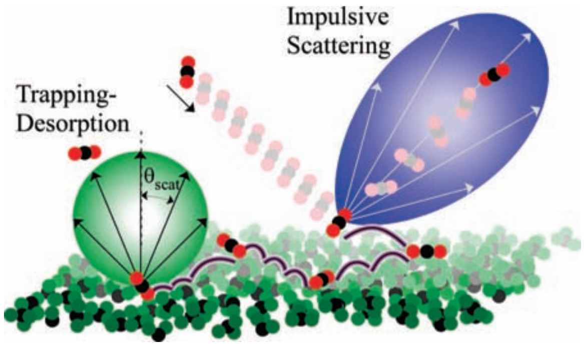

Figure 1. Two classes of collision channels at the gas−liquid interface; (a) trapping desorption (TD), whereby full equilibration to the surface temperature occurs prior to re-entry into the gas phase, and (b) impulsive scattering (IS), which occurs on a sufficiently few collision time scale to yield flux out of equilibrium with the surface temperature. Translational and internal quantum state distributions measured at a series of incident and scattering angles provide evidence for the presence of both TD and IS channels.

[†] Part of the "Stephen R. Leone Festschrift".

* To whom correspondence should be addressed. E-mail: djn@jila.colorado.edu.

10.1021/jp8022887 CCC: $40.75

projectiles, additional and quite complementary information should be present in the internal quantum state distributions of the scattered species. Uncovering this information has been a thrust of recent work in our laboratory, where direct absorption spectroscopy with high-resolution lasers has been exploited to examine rotational and vibrational quantum states resulting from such inelastic[16−19,21] or reactive[20] scattering events. However, additional detailed information on the gas−liquid collision dynamics can be obtained by combining high-resolution lasers with 3D manipulation of the absorbing laser beam path. Specifically, these experiments offer the tantalizing prospect for probing internal state populations of scattered species as a function of incident and final scattering angles, which represents the major focus of the present work.

The primary goal of previous studies has been to explore relevant physical and chemical properties that determine whether or not a gas molecule sticks to a liquid surface. Pioneering TOFMS experiments in the Nathanson group have explored a range of important system parameters, which include incident energy,[45,46] surface temperature,[47,48] and the structure of the gas and surface.[45,46,49−51] Further investigation of the surface structure has been achieved by the development of self-assembled monolayer surfaces (SAMs),[52−54] which provide a model liquid-like structure for molecular beam scattering experiments. Chemical control of the SAM surface enables studies probing effects of surface stiffness,[55] mass,[37,39,56] and hydrogen bonding[57] at the surface. In each case, the scattered molecules are detected along the near-specular scattering direction, where TD and IS components are best separated by final kinetic energies. The TD fraction is, by definition, well-described by a Maxwell−Boltzmann velocity distribution, for which the temperature is most often $\approx T_S$, although several light rare-gas projectiles deviate from this trend.[36,37,40,44] In comparison, the IS molecules typically cover a broader range of final energies and retain a greater fraction of the incident energy. The nature of the IS component reveals a surface with considerable local roughness[48] whereby the incident gas samples a wide range of local collision geometries. In parallel with experimental efforts, high-level molecular dynamics simulations have quantitatively reproduced results from many of the experimental liquid and SAM studies.[33,35−42] From these studies, individual trajectories have been investigated and categorized to determine the nature of TD and IS events. For example, the fraction of molecules that thermally accommodate with the surface sample a diverse range of interactions, which include not only physisorption and solvation pathways but also direct scattering trajectories with one inner turning point. In parallel, analysis of the IS fraction also reveals the importance of single, double, and multiple interactions with the surface, all of which lead to the broad final energy distributions noted in experiments.[35−39]

In an effort to detect gas flux over a broader range of final scattering angles, the Minton group has incorporated a moveable TOFMS to measure various in-plane and out-of-plane scattering geometries for systems such as $O + C_{30}H_{62}$ (*l*).[32,58−60] The TOF technique detects both inelastic O scattering along with reactive scattering of OH and H_2O products. The in-plane measurements covered a range of final scattering angles from $\theta_{scat} \approx -15°$ to 85°, where both the inelastic and reactive products exhibited TOF kinetic energy distributions characteristic of two-channel (TD and IS) dynamics. In each case, the TD component, as defined by kinetic energy distributions, was found to desorb with a $\cos(\theta_{scat})$ angular distribution. In contrast, the impulsive component scatters from the surface in a more directional ("lobular") yet subspecular distribution, which approximately follows a $\cos^n(\theta_{scat} - \theta')$ pattern, where $n \approx 4-6$ and $\theta' < \theta_{spec} = 60°$. Such directionally lobular patterns are strongly suggestive of direct scattering dynamics, that has been extensively investigated in many gas−metal surface systems.[61,62] However, there are also key dynamical differences between gas−liquid and gas−metal scattering studies. For example, laser-based detection of NO + Ag(111)[62] also reveals similar lobular angular distributions but where the recoiling flux now peaks in the superspecular direction. The above comparisons underscore the value of correlated angular and quantum state distributions for further clarifying the role of gas−liquid collision dynamics in both TD and IS scattering channels.

The coupled angular and quantum state distributions provide useful insight into scattering dynamics at the gas−liquid interface. To uncover the TD and IS angular distributions, we first consider results from earlier studies in addition to the laws of detailed balance. For CO_2 scattering from PFPE, we previously determined the incident energy dependence of the TD fraction, which smoothly decreases from unity to ≈ 0.5 as E_{inc} increases from 1.6 to 10.6 kcal/mol.[17] To further investigate CO_2 desorbing from a perfluorinated surface, additional studies at low collision energies ($E_{inc} = 1.6$ kcal/mol) show unity sticking over a range of surface temperatures ($T_S = 232-323$ K).[19] Results of these experiments indicate that scattered CO_2 is well-characterized by Maxwell−Boltzmann rotational and translational distributions where the characteristic temperature is that of the surface, T_S. By detailed balance, unity sticking coefficients and complete thermal accommodation also imply that the angular distribution of the scattered flux (F_{TD}) will follow a $\cos(\theta_{scat})$ distribution,[63] typical of effusion through a small orifice and illustrated in Figure 1. Our experimental results have been quantitatively supported by MD simulations of CO_2 + F-SAMs,[19,35] where the fluorinated self-assembled monolayer has successfully modeled the PFPE interface. Simulations with a $T_S = 300$ K surface show that the total flux from low collision energy trajectories ($E_{inc} = 3.0$ kcal/mol) follows a $\cos(\theta_{scat})$ angular distribution and is characterized by a rotational temperature of ≈ 300 K.[35] The $\cos(\theta_{scat})$ scattering pattern observed under conditions of unity sticking probability simply reflect, again by detailed balance, the uniform angular sampling of collisions at the liquid surface from the gas phase.

Nonequilibrium scattering dynamics that naturally arise at higher incident energies can lead to nonunity sticking probabilities for CO_2 off PFPE. This makes it challenging to unambiguously identify trajectories as TD versus IS pathways. However, by detailed balance, the TD component will be thermally accommodated at T_S if the sticking probability is unity for all sufficiently low incident E_{inc} (say, 0 to $\approx 5RT_S$) represented in the subsequently desorbing flux. Details of this argument are outlined by Rettner, Schweizer, and Mullins, where they model the desorbing flux by the product of $\cos(\theta_{scat})$, a flux-weighted Boltzmann distribution at T_S, and an energy-dependent sticking coefficient.[64] In the case of CO_2 + perfluorinated surfaces at 298 K, we do experimentally observe unity trapping probabilities for normal incident energies up to $5RT_S \approx 3.0$ kcal/mol. Since desorption yields molecules with essentially all energies $< 5RT_S$, then a unity sticking coefficient up to $5RT_S$ necessarily translates into an outgoing TD flux with kinetic and internal energies well-characterized by a Boltzmann distribution at T_S. Furthermore, previous gas−liquid scattering studies even under nonequilibrium conditions by Minton and co-workers demonstrated that the TD component (as measured by time-of-flight) follows a $\cos(\theta_{scat})$ distribution,[32,36,60] sup-

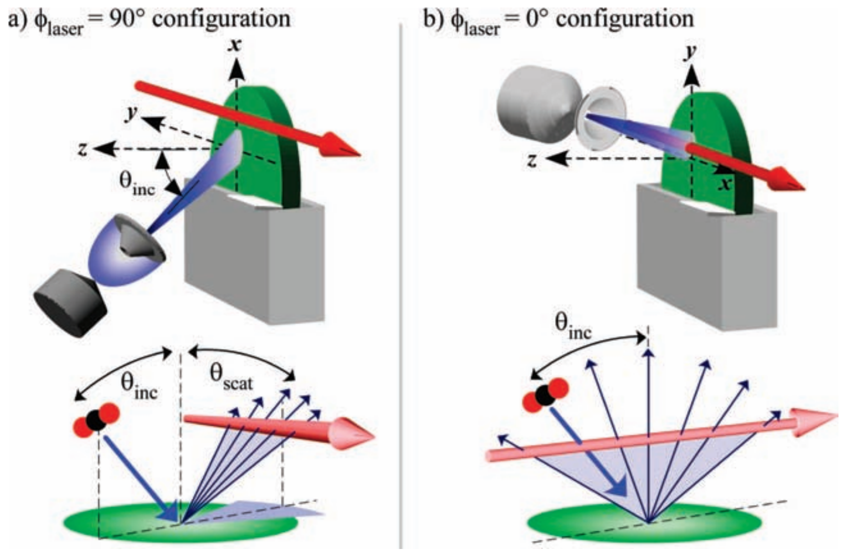

Figure 2. Experimental configuration used to probe CO_2 scattering from a liquid surface, based on high-resolution Pb-salt diode laser absorption. (a) The $\varphi_{laser} = 90°$ configuration permits detection of in-plane ($|\nu - \nu_0| \approx 0$) and out-of-plane ($|\nu - \nu_0| > 0$) scattering events as a function of incident (θ_{inc}) and final angles (θ_{scat}). (b) The $\varphi_{laser} = 0°$ configuration samples exclusively in-plane scattering events, with additional information on forward/backward angular recoil dynamics from high-resolution Dopplerimetry.

porting a unity sticking coefficient independent of angle at near-thermal energies.

On the basis of these considerations, we empirically characterize the TD channel as the fraction of collision events which emerge with (i) internal state distributions equilibrated to T_S and (ii) angular distributions proportional to $\cos(\theta_{scat})$. This is consistent with a physical picture of the fraction of scattering trajectories spending sufficient time near the liquid interface to lose all memory of incident collision conditions. Such a definition also permits us to characterize the (i) angular, (ii) internal quantum state distributions, and (iii) relative branching ratios for flux into the complementary IS channel. Though there is considerable experimental support for this as the simplest description consistent with the data, we note that there is no *a priori* reason why nonequilibrium scattering dynamics should be adequately represented by a simple sum of TD and IS components. Indeed, one can anticipate that deviations from such a two-channel model will eventually be evident at the quantum-state-resolved level, which provides further motivation for continued study with high-resolution IR laser spectroscopic methods.

The present paper focuses on quantum-state-resolved CO_2 scattering from a perfluorinated liquid, where relative TD and IS populations are extracted as a function of incident and scattering angle in an effort to reconstruct the three-dimensional scattering distribution. The remaining sections of this paper include a detailed description of the scattering experiment, which is presented in section II. In section III, quantum state populations are reported for normal and glancing incidence conditions. These results are analyzed with a two-temperature Boltzmann model that incorporates TD and IS dynamics. Section IV includes a discussion of the results, where we present and test a model for the two-channel dynamics. Final remarks and conclusions are summarized in section V.

II. Experimental Section

As illustrated in Figure 2, the experiment consists of a molecular beam of CO_2 impinging upon a renewable liquid surface in vacuum, with scattered molecules detected by direct absorption of infrared laser light with a Pb-salt diode laser spectrometer. Detailed discussion of the apparatus has been presented elsewhere.[16] Therefore, we focus on aspects essential to the current studies, in particular, collision and detection geometries used to probe the scattering dynamics. The incident CO_2 molecules are prepared in a supersonic expansion, where a 10% mixture of CO_2 in hydrogen at 300 K passes through a 500 μm pinhole aperture on a piezo-controlled pulsed valve.[65] The valve generates 300 μs long gas pulses, which pass through a 3.0 mm skimmer positioned 1.5 cm down the expansion axis. The skimmed molecular beam travels an additional 8.5 cm before it impinges upon the liquid surface, which for our current study, we use Krytox 1506 perfluoropolyether (PFPE) as our target liquid. The bulk properties of PFPE listed in Table 1 reveal important criteria for our scattering experiments, which includes low vapor pressure to ensure our laser detection scheme measures nascent scattering populations. In addition, the perfluorinated chemical composition promotes impulsive scattering compared to similar hydrocarbon liquids like squalane.[17,45,46] A freshly renewed PFPE surface is generated by rotating a 15 cm glass wheel through a 200 mL reservoir of liquid, where the liquid is viscously dragged onto the wheel.[66] A razor blade scrapes away impurities at the surface to leave behind a 0.5 mm thick liquid surface. The molecular beam and liquid wheel assembly are housed in a 60 L aluminum vacuum chamber that is equipped with a 6 in. liquid-N_2-cooled diffusion pump. The

TABLE 1: Properties of Bulk PFPE Liquid

	PFPE
chemical composition	$F\text{-}[CF(CF_3)CF_2O]_{14}{}^{a}\text{-}CF_2CF_3$
mass[a]	2400 amu
density	1.87 g/cm^3
melting point	−45 °C
boiling point	200 °C
vapor pressure[b]	7×10^{-7} Torr
viscosity[b]	80 cp
compressibility	10^{-9} cm^2/dyne
surface tension[b]	17 dyne/cm
K_H[c]	3.1×10^4 Torr

[a] Average size of Krytox 1506 polymer. [b] 25 °C. [c] Henry's law constant for CO_2 with $C_{10}F_{22}O_2$.

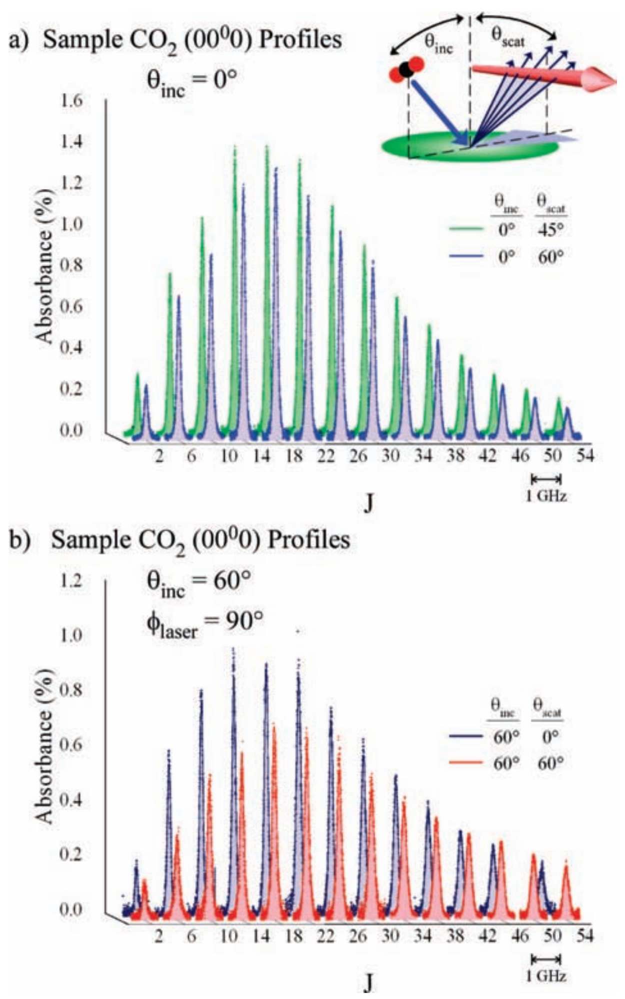

Figure 3. Sample high-resolution CO_2 absorption profiles for incident scattering angles of (a) $\theta_{inc} = 0°$ and (b) $\theta_{inc} = 60°$ for the $\varphi_{laser} = 90°$ laser configuration. $E_{inc} = 10.6(8)$ kcal/mol is achieved by seeding CO_2 in H_2 (300 K) for all experiments reported in the study.

TABLE 2: Two-Temperature Boltzmann Analysis[a] of CO_2 + PFPE; $\varphi_{laser} = 90°$

θ_{inc}[b]	θ_{final}	α	T_{rot}(IS) (K)	T_{vib} (K)
0°	0°	0.56(4)[c]	720(20)	235(4)
0°	30°	0.57(3)	720(30)	234(5)
0°	45°	0.56(3)	730(30)	241(4)
0°	60°	0.56(3)	720(20)	231(5)
30°	−60°	0.62(3)	670(80)	237(4)
30°	−30°	0.57(3)	830(70)	232(5)
30°	0°	0.56(2)	830(60)	231(2)
30°	30°	0.51(3)	860(40)	237(5)
30°	60°	0.38(2)	710(40)	235(2)
45°	−60°	0.61(4)	740(80)	233(5)
45°	−30°	0.60(5)	780(90)	228(7)
45°	0°	0.53(2)	940(80)	238(8)
45°	30°	0.49(2)	950(60)	234(5)
45°	45°	0.42(2)	940(60)	247(5)
45°	60°	0.32(2)	820(40)	238(5)
60°	−60°	0.67(6)	800(160)	229(9)
60°	−30°	0.49(4)	880(110)	232(5)
60°	0°	0.40(7)	790(30)	235(5)
60°	30°	0.32(3)	810(30)	243(9)
60°	60°	0.29(3)	1220(40)	238(9)

[a] T_{rot}(TD) is fixed at T_S = 298 K in the nonlinear least-squares fit. [b] Configuration is illustrated in Figure 2a. [c] Numbers in parentheses represent the estimated error from the two-temperature fit over several data sets.

operating pressure is maintained at 3 × 10^{-5} Torr, while the pulsed valve operates at 11 Hz with a backing pressure of 100 Torr.

CO_2 molecules are detected with a Pb-salt diode laser spectrometer by direct absorption on the ν_3 asymmetric stretch. The tunable laser produces 1−2 μW of light at around $\lambda = 4.2$ μm, which covers rovibrational transitions for CO_2 in the ground (00^00; $J = 0-54$) and first bend-excited (01^10; $J = 0-38$) vibrational states.[67] The laser is coarsely tuned via a commercial temperature controller ($\Delta\nu/\Delta T \approx 3-4$ cm^{-1}/K) and finely tuned with a low noise current source ($\Delta\nu/\Delta I \approx 2$ MHz/μA). Within the spectrometer, the beam is split at several points to simultaneously measure the absorption of the scattered molecules as a function of laser frequency. First, the absolute frequency is established from absorption of a reference gas, while the relative frequencies are determined from interpolation of transmission fringes from a confocal etalon. The remaining fraction of the original beam is used to detect the scattered gas molecules. The beam is split, where the first half is passed above the liquid surface in a multipass configuration,[68] after which it is directed onto a liquid-N_2-cooled InSb photovoltaic detector. A reference InSb detector records the second fraction of the light, at which point, the signals from both detectors are sent to fast servo-loop subtraction electronics to eliminate common mode noise. The detection scheme results in absorption sensitivities of 1−2 × 10^{-6} $Hz^{-1/2}$. The combined signal is sent to a computer-controlled A/D, where the time signals are stored as a function of detuning frequency. The time signals include a 2 ms fragment that incorporates windows before, during, and after the gas pulse collides with the surface. IR frequency-dependent Doppler absorption profiles are generated from these signals by integration over the rising edge (∼200 μs) of the scattered gas pulse.

As depicted in Figure 2, multiple configurations are used to detect the scattered flux over a range of final angles. For experiments reported in this study, the molecular beam impinges upon the surface with incident angles (θ_{inc}) of 0°, 30°, 45°, and 60°, where θ_{inc} is defined as the angle between the expansion axis of the molecular beam and the surface normal (z-axis). For convention, the molecular beam axis starts in the $x-z$ plane, which then places the laser propagation direction parallel to the y-axis in the $\varphi_{laser} = 90°$ configuration (Figure 2a) or parallel to the x-axis in $\varphi_{laser} = 0°$ (Figure 2b). For each configuration, the final scattering angle (θ_{scat}) depends upon the spatial relationship between the spot of the molecular beam on the surface with the position of the laser multipass. At the $\varphi_{laser} = 90°$ configuration, θ_{scat} is the in-plane scattering angle where the laser detects molecules that are traveling in the $x-z$ plane (i.e., $v_y = 0$; $\varphi_{scat} = 0°$). Additionally, the schematic in Figure 2a shows that the laser can detect out-of-plane scattering due to Doppler-shifted absorption at detuning frequencies that correspond to $\Delta\nu/\nu_0 = v_y/c$. The laser detection scheme also provides opportunity to measure both forward and backward scattering as we change the configuration from $\theta_{scat} = -60°$ to +60°. In each case, the radial distance from the laser beam (θ_{scat}; $\varphi_{scat} = 0°$) to the center of the molecular beam spot on the surface is fixed at 2.0 cm. By way of comparison, the $\varphi_{laser} = 0°$ configuration exclusively detects in-plane scattering, including both forward and backward directions. This pair of configurations therefore provides a unique opportunity to simultaneously extract internal quantum state, angular, and velocity component information for both in-plane and out-of-plane scattering in the forward and backward directions.

III. Results

A. Incident Beam Characterization. Prior to each scattering experiment, the molecular beam is characterized in the absence of the liquid wheel assembly. First, absorption profiles, $A(\nu - \nu_0)$, are recorded for a series of J states within each vibrational manifold. Each profile is sampled over all detuning frequencies to generate column-integrated densities ($A_{v,J}$) for the internal state population, which is directly proportional to the density in a particular quantum state, $\rho_{v,J}(x,y,z)$. Explicitly

$$A_{v,J} = \int A(\nu - \nu_0)\mathrm{d}\nu = S_{v,J} \int \rho_{v,J}(x, y, z)\mathrm{d}y \qquad (1)$$

where $S_{v,J}$ is the Hönl−London line strength for a given transition.[69] To characterize the internal state distribution, the column densities are divided by $S_{v,J}$, $(2J + 1)$ degeneracy, and plotted against $E_{\mathrm{rot}} = B_{\mathrm{CO_2}}J(J + 1)$ in a standard Boltzmann fashion. The best-fit line to the data represents the rotational temperature (T_{rot}), which is ≈15 K for the supersonically cooled CO_2 in the molecular beam. A comparison of the relative populations in the 00^00 and 01^10 manifolds reveals a simple estimate of ≈175 K for the vibrational temperature (T_{vib}). The dramatic differences in temperatures for these two degrees of freedom clearly reveal the difficulties of relaxing a 667 cm^{-1} vibrational mode compared to rotational levels[70] that are spaced at intervals of $2B_{\mathrm{CO_2}}J$, where $B_{\mathrm{CO_2}} \approx 0.3902\ \mathrm{cm}^{-1}$.

In addition to internal state characterization, the total kinetic energy of the molecular beam is characterized before the scattering experiments. The translational degrees are characterized using time-of-flight measurements and high resolution Dopplerimetry of the absorption profiles. First, a hearing aid microphone is used in a TOF experiment where the gas pulse arrival time is measured for a series of distances along the expansion axis,[71] with a distance versus time plot yielding an average velocity for the pulsed molecular beam. The measured velocity is $1.41(9) \times 10^5$ cm/s, which agrees well with the calculated value of 1.42×10^5 cm/s from standard gas flow formulas.[70] From this velocity, we calculate the incident energy of the CO_2 to be $E_{\mathrm{inc}} = 10.6(8)$ kcal/mol. Additional translational characterization involves line shape fits to the absorption profiles, which provide distributions for the orthogonal translational degrees. First, absorption profiles from the $\theta_{\mathrm{inc}} = 0°$ configuration are fit to a Voigt line shape, where the Gaussian component models the velocity spread due to the skimmer, while the Lorentzian width simply accounts for a finite residual line width of the laser ($\Delta\nu_{\mathrm{L}} \approx 20$ MHz).[16] The extracted Doppler width ($\Delta\nu_{\mathrm{D}} \approx 66(4)$ MHz) agrees well with calculated fwhm velocity distributions based on the geometry of the skimmer ($\theta_{\mathrm{fwhm}} \approx 12°$) and average centerline speed of the molecular beam. Beyond normal incidence, $\theta_{\mathrm{inc}} = 30°$, 45°, and 60° in the $\varphi_{\mathrm{laser}} = 0°$ configuration produce a line shape that consists of two Gaussians, each symmetrically offset from the rest transition frequency (ν_0). While the symmetry is due to the laser multipass, the offset reflects the projection of the centerline velocity along the laser propagation direction. The extracted shifted frequencies for $R(0)$ are ±159(4), ±228(2), and ±286(2) MHz for $\theta_{\mathrm{inc}} = 30°$, 45°, and 60°, respectively. Similar values are obtained for other J state absorption profiles, after which a simple calculation turns these frequency projections into centerline velocities of $1.32(4) \times 10^5$, $1.35(9) \times 10^5$, and $1.39(4) \times 10^5$ cm/s. While each of these values is similar to our microphone TOF characterization, the values all deviate to the slow side of the TOF average, which is consistent with velocity slip effects in the pinhole expansion.[70]

B. Normal Incidence Scattering. The simplest scattering geometry involves CO_2 impinging on the surface at normal incidence. With a fixed incident angle of $\theta_{\mathrm{inc}} = 0°$, the first series of experiments consist of measuring the J state populations at scattering angles of $\theta_{\mathrm{scat}} = 0°$, 30°, 45°, and 60°. Sample absorption profiles are illustrated in Figure 3a for scattered CO_2 (00^00) at $\theta_{\mathrm{scat}} = 45°$ and 60°, providing the opportunity to compare distributions for two different final angles. The differences between the two probe geometries are minor, where the general shape of the envelope is essentially the same. The only qualitative difference is that the overall amplitude of the absorption for $\theta_{\mathrm{scat}} = 45°$ is ∼10% larger than that for $\theta_{\mathrm{scat}} = 60°$. To make this comparison more quantitative, we turn to a two-temperature Boltzmann analysis previously used to characterize scattered quantum state populations.

As outlined in the previous section for the incident beam characterization, we integrate the absorption profiles to create column densities that then are fit with a two-temperature Boltzmann model.[16] The model assumes that the total population is the sum of two subpopulations, TD and IS, where each component is well-characterized by a temperature, T_{rot}(TD/IS). The model also assumes that the 00^00 and 01^10 populations are described by the same rotational temperatures but differ by T_{vib}. Explicitly, the populations are fit to the following function

$$\frac{A_{v,J}}{S_{v,J}} = N\cdot\{\alpha\cdot P_{\mathrm{TD}}(J) + (1-\alpha)\cdot P_{\mathrm{IS}}(J)\}\cdot P_{\mathrm{vib}}(v) \qquad (2)$$

where α is the density-based trapping desorption fraction at a given probe geometry (θ_{scat}, φ_{laser}) and $P_{\mathrm{TD/IS}}(J)$ and $P_{\mathrm{vib}}(v)$ are the standard Boltzmann probability distributions

$$P_{\mathrm{TD/IS}}(J) = \frac{(2J+1)\cdot \mathrm{e}^{-E_{\mathrm{rot}}/kT_{\mathrm{rot}}(\mathrm{TD/IS})}}{Q_{\mathrm{rot}}(\mathrm{TD/IS})} \qquad (3)$$

$$P_{\mathrm{vib}}(v) = \frac{\mathrm{e}^{-h\nu/kT_{\mathrm{vib}}}}{Q_{\mathrm{vib}}} \qquad (4)$$

Populations are fit to eq 2 with a nonlinear least-squares algorithm, where the T_{rot}(TD) is fixed at 298 K to reduce parameter correlation. As noted in the Introduction, we have explicitly tested this assumption in previous studies[19] where low collision energy scattering results in unity sticking and rotational temperatures that equal the surface temperature. Extracted values from the fit are summarized in Table 2.

Quantum state populations for each scattering angle are plotted in Figure 4a for normal incidence. Results from the two-temperature fit are used to normalize the populations, which enables us to compare the relative distribution of the population as a function of scattering angle. In addition to experimental data and two-temperature fit, individual TD and IS components are simultaneously plotted as green and blue curves, respectively, for each θ_{scat} in Figure 4a. As a qualitative assessment of similarities and differences, an arrow marks the J state that corresponds to where the total population is equally divided between TD and IS components. This matching point remains constant at $J \approx 34$ for each θ_{scat}, which indicates qualitatively similar distributions over all final scattering angles.

To compare the dynamics more quantitatively, we plot the TD fraction (α) as a function of θ_{scat} in Figure 5a. Remarkably, the polar plot reveals that α remains nearly constant from $\theta_{\mathrm{scat}} = 0°$ to 60°, with the points along the gray dashed curve denoting a fixed average value of α = 0.56. In addition, the extracted T_{rot}(IS) values are plotted in Figure 5b, which indicates that the IS rotational temperatures also remain nearly constant at $T_{\mathrm{rot}}(\mathrm{IS}) = 720$ K for each θ_{scat}. Finally, the two-temperature

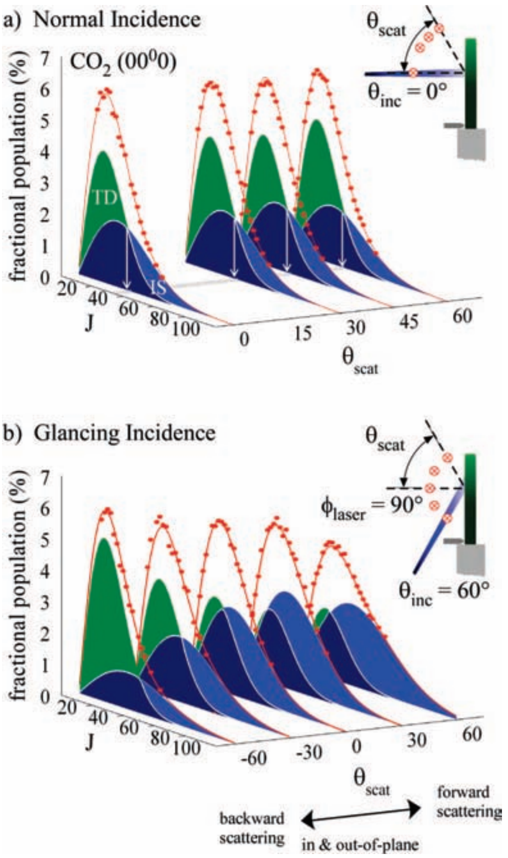

Figure 4. Rotational state populations for scattered CO_2 (00^00) under (a) normal incidence ($\theta_{inc} = 0°$, $\theta_{scat} = 0°, 30°, 45°, 60°$) and (b) non-normal incidence ($\theta_{inc} = 60°$, $\theta_{scat} = -60°, -30°, 0°, 30°, 60°$) conditions, each with a $\varphi_{laser} = 90°$ probe configuration. In all cases, the dynamics can be characterized by a two-temperature Boltzmann analysis, with two populations (TD and IS) quantitatively described by rotational temperatures, T_{rot}(TD) and T_{rot}(IS). Remarkably little dependence in the TD/IS distributions on final scattering angle is noted at normal incidence, consistent with $\cos(\theta_{scat})$ angular distributions for both TD/IS channels (see text for details). Conversely, strong growth in the IS versus TD fraction with increasing angle for non-normal incidence scattering is clearly evident, consistent with a propensity for lobular scattering in the forward (though slightly subspecular) direction.

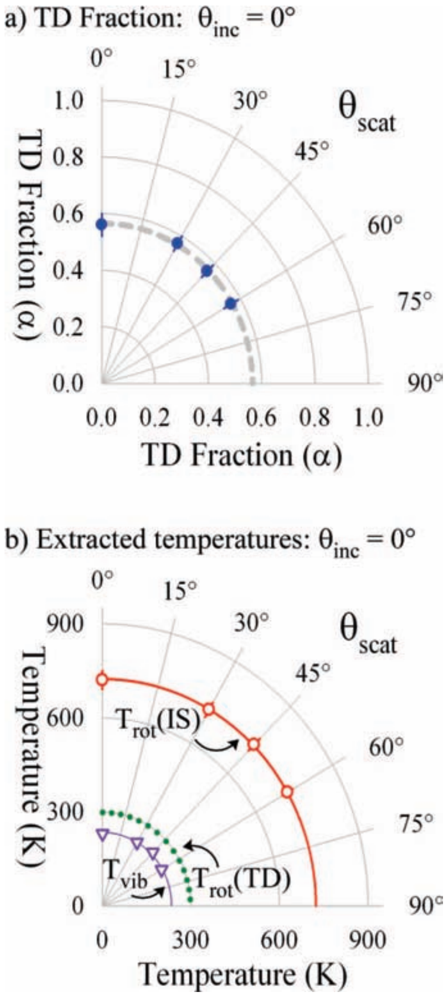

Figure 5. Least squares two-temperature Boltzmann fit parameters for normal incidence scattering ($\theta_{inc} = 0°$) and $\varphi_{laser} = 90°$ probe configuration. (a) Trapping desorption fraction, α, obtained from fits in Figure 4a. b) Fitted IS and TD rotational temperatures as well as vibrational temperatures over the same range of scattering angles. Note the essentially complete independence of all of these parameters on θ_{scat}, again consistent with identical $\cos(\theta_{scat})$ angular distributions for both TD/IS channels under normal incidence conditions.

analysis indicates negligible $T-V$ vibrational excitation based on a nearly constant (and sub-T_S) vibrational temperature of $T_{vib} \approx 235$ K.

One experimental issue is finite angular resolution due to the size of the laser beam multipass. This motivated an independent series of experiments at fixed $\theta_{inc} = 60°$, for distances varying from 2 to 8 cm from the liquid wheel. The increased distance yielded a four-fold improvement in angular resolution of the laser detection scheme (to $\pm\approx 4°$), with no influence on the measured populations within statistical uncertainty. On the basis of the azimuthal symmetry of the normal incidence geometry, we can model the scattered IS angular distributions by $F_{IS} \propto \cos^n\theta_{scat}$, where n is determined from experiment. Further details will be presented in section IV, but the limited change in α as a function of θ_{scat} implies that the ratio between the TD flux and IS flux is constant over all final scattering angles. Since we know that $F_{TD} \propto \cos\theta_{scat}$, the constant value of α suggests a similar (i.e., $n \approx 1$) angular distribution for both TD and IS scattering at normal incidence.

C. Incident Angle Effects at $\varphi_{laser} = 90°$. While normal incident scattering from the liquid surface necessarily yields symmetric angular distributions around the surface normal, $\theta_{inc} > 0°$ introduces an asymmetry that permits preferential scattering in certain directions, for example, forward, backward, in-plane, or out-of-plane. As a first step toward characterizing these angular distributions, we use the $\varphi_{laser} = 90°$ experimental configuration illustrated in Figure 2a, for which the laser beam is normal to the scattering plane. Sample absorption profiles are plotted in Figure 3b for $\theta_{inc} = 60°$ scattering (i) normal to the surface ($\theta_{scat} = 0°$) and (ii) forward toward the specular direction ($\theta_{scat} = 60°$). In terms of internal state populations, the manifolds once again show smooth, temperature-like distributions over all J states. However, the two angles clearly exhibit contrasting results, where the forward scattering events ($\theta_{scat} = 60°$) preferentially populate the higher rotational states. It is important to keep in mind that for the $\varphi_{laser} = 90°$ geometry, each high-resolution Doppler profile contains information on both in-plane ($\nu - \nu_0 \approx 0$ MHz) and out-of-plane ($|\nu - \nu_0| > 0$ MHz) scattering signals, sorted by detuning from the rest frequency. Detailed analysis of these absorption profiles as a function of θ_{scat} permits the true 3D state-resolved flux distributions to be determined, the results of which will be presented elsewhere.[72] However, to maintain consistency with the two-temperature analysis of the previous section, at this point, we simply integrate the Doppler profiles and sum over all out-of-plane y-velocity components.

The integrated absorption profiles yield absolute column densities, which reflect both in-plane and out-of-plane scattering contributions into a given quantum state. Once again, the data are fit to eq 2 for each $\theta_{inc}/\theta_{scat}$ experiment to extract α, T_{rot}(TD/IS), and T_{vib}. The TD rotational temperature is fixed at $T_{TD} = T_S \approx 298$ K since the internal state distribution of CO_2 is assumed to be independent of θ_{scat}. Additionally, our model characterizes the final IS distributions with a temperature, T_{rot}(IS), that may or may not depend on the final scattering angle. Results from these fits are used to normalize the populations for a given configuration, which is illustrated for five detection angles in Figure 4b for $\theta_{inc} = 60°$. Even cursory examination of these distributions shows dramatic contrast in comparison with the normal incidence ($\theta_{inc} = 0°$) scattering populations noted previously in Figure 4a. Specifically, populations for backscattered CO_2 ($\theta_{scat} < 0°$) are significantly concentrated into lower J states, which results in a relatively large TD component (green curve) inferred for these scattering angles. Conversely, the forward scattering experiments ($\theta_{scat} > 0°$) exhibit distributions with population shifting toward higher rotational states, indicating a systematic evolution of TD (green curve) to IS (blue curve) as a function of scattering angle. Preferential forward scattering for IS trajectories indicates a surface interaction in which a significant component of the incident CO_2 momentum is conserved. Detailed analysis of α and T_{rot}(IS) in the following paragraphs provides further insight into these interactions and the ways in which they evolve as a function of θ_{inc}.

We first plot α against θ_{scat} in Figure 6a for $\theta_{inc} = 0°$, 30°, 45°, and 60° to uncover quantitative trends in the scattering distributions. Results for each θ_{inc} are compared over $\theta_{scat} = -60°$ to $+60°$, where values from Figure 5 have been included for $\theta_{inc} = 0°$. For this specific angle, values for α at a given θ_{scat} are also plotted at $-\theta_{scat}$ since both angles ($\pm\theta_{scat}$) are equivalent due to azimuthal symmetry for a normal incidence geometry. The gray dashed line behind the data points reflects the observed value (α = 0.56) in this polar plot (see section IIIB) inferred experimentally for F_{TD}, $F_{IS} \propto \cos\theta_{scat}$. While the sticking probability follows this curve nicely for $\theta_{inc} = 0°$, the experimentally extracted TD fractions deviate significantly from the curve as θ_{inc} increases to 30°, 45°, and 60°. The deviations are most clearly illustrated at $\theta_{inc} = 60°$, for which the trapping probability decreases from α ≈ 67% to 29% for backward ($\theta_{scat} = -60°$) to forward ($\theta_{scat} = 60°$) scattering, respectively. Such an angular dependence in α is also apparent for other non-normal incident conditions, with the effects simply more dramatic as θ_{inc} increases.

In addition to sticking probabilities, IS rotational temperature T_{rot}(IS) values extracted as a function of θ_{scat} provide complementary information on the scattering dynamics. The temperatures plotted in Figure 6b reveal several interesting trends worth noting. First, T_{rot}(IS) results for $\theta_{inc} = 0°$ are again plotted to illustrate the near-angular independence of the two-temperature dynamics as a function of θ_{scat}. The similar θ_{scat}-independent trends in α and T_{rot}(IS) at $\theta_{inc} = 0°$ are consistent with an IS channel that includes single to several collisions between the gas and liquid at the interface. These interactions are sufficient to excite the CO_2 into a hot, yet Maxwell−Boltzmann (i.e., thermal), distribution of rotational states, where molecules impinging at normal incidence sample adequate surface roughness to scatter into a random (i.e., $\cos^n(\theta_{scat})$, $n \approx 1$) distribution of recoil directions. Beyond $\theta_{inc} = 0°$, however, T_{rot}(IS) for CO_2 systematically increases for all final scattering angles, with degree of additional rotational excitation strongly correlated with incident angle. In particular, the largest glancing incident angles ($\theta_{inc} = 60°$) result in the hottest rotational distributions where IS temperatures reach ≈1200 K. This trend in T_{rot}(IS) would be qualitatively consistent with surface roughening at the gas−liquid interface, where glancing angles would be more likely to torque molecules into higher rotational states. Once again, however, in stark contrast to the strong incident angular dependence of rotational excitation, the vibrational temperatures listed in Table 2 reveal essentially no dependence on this degree of freedom. For each angle, T_{vib} remains well below $T_S = 298$ K, which indicates a very inefficient flow of energy into the bending mode of CO_2 on the time scale of a collisional event.

a) TD Fraction (α): $\phi_{laser} = 90°$

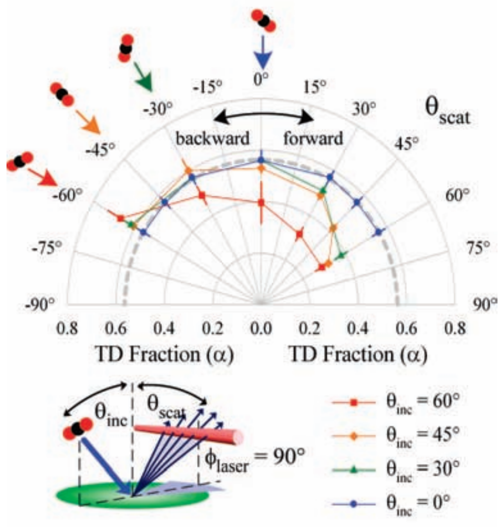

b) Extracted temperatures: $\phi_{laser} = 90°$

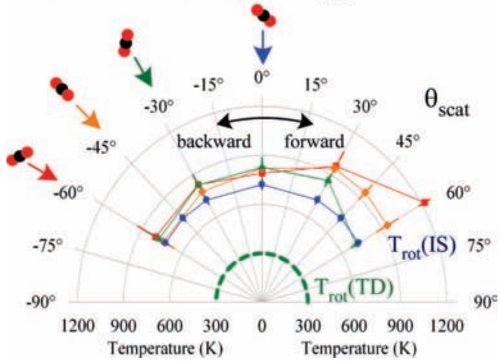

Figure 6. (a) Trapping desorption fraction, α, as a function of θ_{scat} for $\theta_{inc} = 0°$, 30°, 45°, and 60° for a $\varphi_{laser} = 90°$ configuration. The gray dashed line reflects α = 0.56, which is the average value for normal incidence experiments. This line also reflects the trapping desorption fraction predicted if the IS component scatters with a $\cos(\theta_{scat})$ angular distribution (see text for details). (b) Fitted IS rotational temperatures as a function of θ_{scat} for $\theta_{inc} = 0°$, 30°, 45°, and 60°. Note the systematic increase in T_{rot}(IS) with increasingly non-normal angle of incidence.

D. Incident Angle Effects at $\varphi_{laser} = 0°$. The laser detection scheme also permits measurement of scattered CO_2 in the $\varphi_{laser} = 0°$ experimental configuration depicted in Figure 2b. This configuration predominantly samples in-plane scattering dynamics in forward and backward directions, where high-resolution Doppler profiles provide further evidence for TD and IS populations. Sample absorption profiles for $\theta_{inc} = 60°$ are plotted in Figure 7a along with a cartoon representation of the experimental configuration. From low to high J states, the

a) Sample Progression

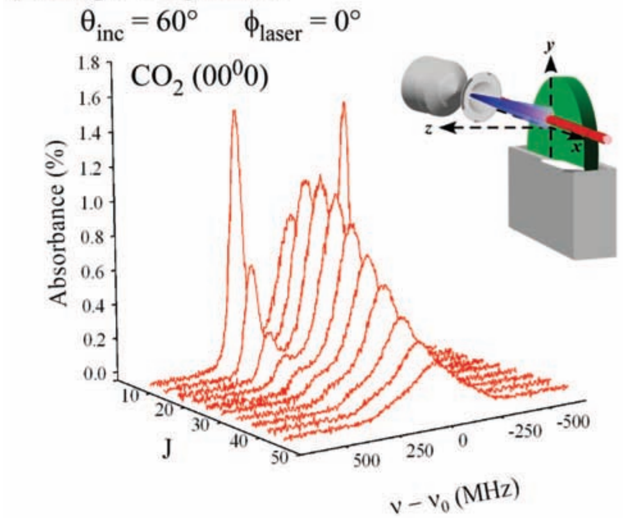

b) Scattered CO_2 Absorption Profile

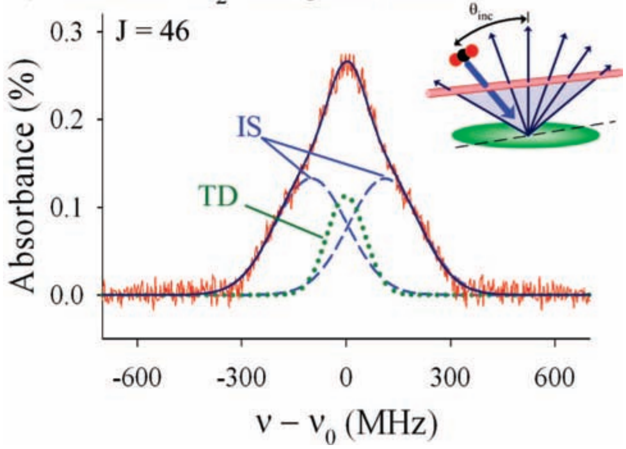

Figure 7. (a) Sample high-resolution absorption profiles measured at $\theta_{inc} = 60°$ in the $\varphi_{laser} = 0°$ configuration for a series of final rotational states. (b) A closer look at the Doppler profile for CO_2 rotationally excited into $J = 46$, along with the least-squares fits into individual TD (green dot) and IS (blue dash) components. Preliminary high-resolution analysis is consistent with a TD component equilibrated to the surface temperature (T_S), with a forward/backward-scattered IS component moving with respect to the surface at $\langle |v_x| \rangle = 3.9(1) \times 10^4$ cm/s.

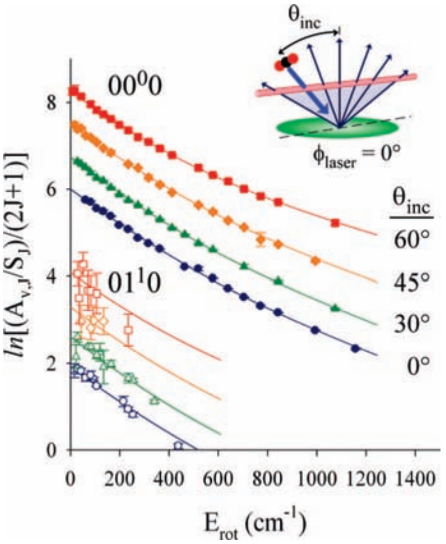

Figure 8. Sample Boltzmann analysis for ground (00^00) and bend-excited (01^10) vibrational states of scattered CO_2, sampled for $\theta_{inc} = 0°$, 30°, 45°, and 60° and measured in the $\varphi_{laser} = 0°$ configuration. Populations reflect in-plane column scattering densities integrated over all final angles.

progression of profiles reveals a series of complex line shapes that contain velocity component information about the incident and scattered molecules. For example, narrow absorption features at low J are observed at large Doppler-shifted frequencies of ±286 MHz. These are due to residual absorption of the incident beam, which, even though cooled down to $T_{rot} \approx 15$ K, yields small but nonzero absorption contributions with respect to the scattered flux. Indeed, on the basis of the known $\theta_{inc} = 60°$ incident angle, such data provide a useful independent measure of the beam velocity ($v = 1.39(4) \times 10^5$ cm/s), in good agreement with direct time-of-flight measurements ($v = 1.41(9) \times 10^5$ cm/s). At higher J values, the signals are quickly dominated by scattered CO_2 flux, yielding Doppler profiles symmetrically centered on the centerline transition frequency (ν_0). The progression of scattered populations once again shows a temperature-like distribution, where signals increase at low J, reach a maximum at $J \approx 16$, and then decay as J extends into higher states. Analysis of the data must take into account both high-resolution Dopplerimetry of the line shape profiles to extract v_x distributions as well as a two-temperature Boltzmann characterization of the internal state populations.

The sample absorption profile in Figure 7b reveals significant deviations from the Gaussian profiles measured in previous studies.[16−19] The Doppler profiles, which now include broad shoulder-like features symmetrized by the laser multipass geometry, provide direct evidence for both (i) a TD velocity component centered at zero and (ii) a shifted IS velocity distribution with nonzero $\langle v_x \rangle$. The simplest model consistent with the data involves fitting the absorption profiles to a sum of Gaussian functions that correspond to TD and IS components, each of which is described by an amplitude, Doppler width [$\Delta\nu_D$(TD/IS)], and centerline frequency ($\nu_{TD/IS}$). The TD population is characterized by a single Gaussian centered at $\nu_{TD} = 0$ MHz, while the IS component reflects two Gaussian functions symmetrically displaced by $\pm\nu_{IS}$. The TD component desorbs from the surface with a Maxwell−Boltzmann velocity distribution characterized by $T_{trans}(TD) = T_S$, which allows us to directly calculate $\Delta\nu_D$(TD). These parameters permit least-squares extraction of relative TD and IS amplitudes, $\Delta\nu_D$(IS) and ν_{IS}. A sample Doppler fit for $J = 46$ is included in Figure 7b, where the sum of TD and IS components nicely accounts for the shoulder-like features. Extracted fit parameters include $\Delta\nu_D(IS) = 249(5)$ MHz, which is nearly two-fold larger than $\Delta\nu_D(TD) = 129$ MHz and six-fold larger than the incident beam width of $\Delta\nu_D = 66(3)$ MHz. Additionally, the fit yields a shifted IS centerline frequency of $\nu_{IS} = 89(3)$ MHz, which corresponds to an average velocity component in the x-direction of $\langle v_x \rangle = 3.9(1) \times 10^4$ cm/s. This average velocity is much slower than the observed speed in the incident beam and thus is consistent with substantial transfer of kinetic energy into the liquid even for IS trajectories. A complete analysis of these Doppler profiles will require simultaneous least-squares fitting of data for each J state and for both $\varphi_{laser} = 0°$ and $\varphi_{laser} = 90°$ configurations, a task which is presently underway.[72]

In addition to the two-component Doppler profiles, the quantum state populations can be analyzed for $\varphi_{laser} = 0°$ with the two-temperature Boltzmann model to extract sticking probabilities. Relative populations and fits are plotted in Figure 8 for incident beam conditions sampling $\theta_{inc} = 0°$, 30°, 45°,

TABLE 3: Two-Temperature Boltzmann Analysis[a] of CO_2 + PFPE; $\varphi_{laser} = 0°$

θ_{inc}[b]	α	T_{rot}(IS) (K)	T_{vib} (K)
0°	0.56(3)[c]	720 (20)	235(4)
30°	0.59(5)	770(40)	232(2)
45°	0.54(3)	780(60)	228(8)
60°	0.50(4)	920(40)	230(5)

[a] T_{rot}(TD) is fixed at T_S = 298 K in the nonlinear least-squares fit. [b] Configuration is illustrated in Figure 2b. [c] Numbers in parentheses represent the estimated error from the two-temperature fit over several data sets.

and 60°. The semilog plot illustrates the non-Boltzmann behavior expected for gas−liquid scattering, which appears as curvature in the distribution of populations. Fits to the two-temperature model provide least-squares values of α, T_{rot}(IS) and T_{vib}, which are listed in Table 3 and plotted in Figure 9 as a function of θ_{inc}. In stark contrast with the $\varphi_{laser} = 90°$ probe geometry, the TD fraction in Figure 9a demonstrates little change in sticking probability with θ_{inc}; α decreases only very slightly from ≈0.56 to ≈0.50 as θ_{inc} increases from 0° to 60°. Similarly, Figure 9b illustrates that T_{rot}(IS) increases modestly from ≈720 K to ≈920 K over the same range of incident angles. Not unexpectedly, the bending vibration remains a “spectator” coordinate, with T_{vib} nearly constant at ≈230 K for each configuration. Detailed comparison of results from both φ_{laser} = 0° and 90° laser configurations is presented in section IV.

IV. Discussion

A. Modeling IS Angular Distributions at Normal Incidence. Motivated by success of the two-channel Boltzmann fits for $\theta_{inc} = 0°$, we explore a simple physical model to characterize the angular distributions for TD and IS fluxes. Azimuthal symmetry in this scattering geometry limits possible distributions to those that only depend on the final polar angle, θ_{scat}. We extend the two-temperature Boltzmann model to angular distributions, where the total scattering distributions are assumed to be composed of both TD and IS components. By definition, flux from the TD component is given by $F_{TD} \propto \cos(\theta_{scat})$, whereas the IS flux is assumed to follow $F_{IS} \propto \cos^n(\theta_{scat})$, with n treated as a fitting parameter.[63] Representations of these distributions are illustrated in Figure 10a for n = 0.5, 1.0, 2.0, and 4.0. Our treatment implicitly assumes separable angular and rotational contributions to each scattering channel, which allows us to calculate α as a function of θ_{scat} based on model angular distributions. The objective of this analysis is to calculate the TD fraction as a function of θ_{scat} for different values of the exponent (n) to directly compare with the experimentally determined TD fractions presented in section IIIB.

As a first step, we develop a general expression for the flux to column-integrated density transformation. With regard to Figure 10a, flux from a point source with an assumed angular dependence of $\cos^n(\theta_{scat})$ is characterized in spherical coordinates by

$$f(r,\theta,\varphi) = C_n \cdot \frac{\cos^n(\theta)}{r^2} \tag{5}$$

where the proportionality constant, $C_n = (n+1)\cdot I/2\pi$, is determined by equating the integral $\int f(r,\theta,\phi) r^2 \mathrm{d}r \sin\theta \, \mathrm{d}\theta \mathrm{d}\varphi$ over all scattering space to the total flux, I (in molecules/sec). The flux to density transformation requires correction by $1/v_\perp$, where $v_\perp = \sqrt{(v_x^2 + v_z^2)}$ is the velocity component perpendicular to the laser probe axis. Additionally, the laser only detects molecules scattered into the probe column parallel to the y-axis, yielding densities in terms of total intensity (I) and perpendicular velocity ($v_\perp$) in Cartesian coordinates as

$$\rho(x,y,z,v_\perp) = \frac{n+1}{2\pi}\frac{I}{v_\perp}\frac{z^n}{(x^2+z^2)^{1/2}\cdot(x^2+y^2+z^2)^{(n+1)/2}} \tag{6}$$

To compare with experimental measurements, the density in eq 6 must be integrated along the laser propagation direction (y) at a fixed x and z distance from the source, where $\theta_{scat} = \tan^{-1}(x/z)$. The column-integrated density (A) is therefore obtained by numerical integration of

$$A = \int \rho(x,y,z,v_\perp)\mathrm{d}y \tag{7}$$

Numerically computed integral values for eq 7 are plotted in Figure 10b as a function of θ_{scat} for n = 0.5, 1.0, 2.0 and 4.0. High values of “n” clearly result in column-integrated density peaked toward the surface normal, whereas low values of “n” spread the integrated density over a broader range of angles. These normalized column-integrated density distributions enable us to predict how the measured TD fraction (α) depends on $\theta_{scat.}$ Specifically, the TD fraction expressed in terms of $A_{TD/IS}$ is

$$\alpha = \frac{A_{TD}}{A_{TD} + A_{IS}} \tag{8}$$

where the angular distributions for each component are taken to be $\cos(\theta_{scat})$ and $\cos^n(\theta_{scat})$ for A_{TD} and A_{IS}, respectively. Results of these calculated sticking probabilities are plotted in Figure 10c for n = 0.5, 1.0, 2.0, and 4.0 along with the experimentally determined TD fractions. The trends in α over θ_{scat} are clearly sensitive to the value of “n” used to model the IS flux. For example, $F_{IS} \propto \cos^4\theta_{scat}$ exhibits the highest column-integrated densities at normal angles and fastest density drop-off as a function of θ_{scat}. The TD fraction calculated from eq 8 for n = 4 distributions ranges from α ≈ 0.35 to 1.00 as θ_{scat} increases from 0° to 60°, which is plotted in Figure 10c with similar TD curves for other possible IS distributions. However, the least-squares fit curve that most closely matches the IS experimental results corresponds to “n” = 1.0 ± 0.2. Alternatively stated, the experimental data are consistent with a simple physical picture in which the IS channel scatters CO_2 from the PFPE surface after single, double, and multiple interactions into a final angular distribution of $F_{IS} \propto \cos(\theta_{scat})$, that is, indistinguishable from the normal “effusive” TD channel within experimental uncertainty. The nature of the angular and rotational state distributions indicates that CO_2 interacts with a corrugated surface, where roughness is a result of capillary waves and the local chemical structure of the PFPE liquid.[19,47,48]

B. IS Scattering as a Function of Incident Angle. The azimuthal symmetry for normal incidence (θ_{inc} = 0°) beam conditions simplifies the final scattering distributions to be a function only of θ_{scat} and independent of φ_{scat}. However, this symmetry is broken for $\theta_{inc} > 0°$, yielding directional scattering as, for example, clearly evident in the sticking probabilities in Figure 6a for θ_{inc} = 60°. The systematic decrease in α from $\theta_{scat} = -60°$ to +60° indicates that molecules in the IS channel preferentially scatter in the forward direction. This loss of symmetry for $\theta_{inc} > 0°$ introduces significant deviations from our previous simple $\cos^n\theta_{scat}$ characterization of the IS angular distribution. Indeed, more accurate models for these angular

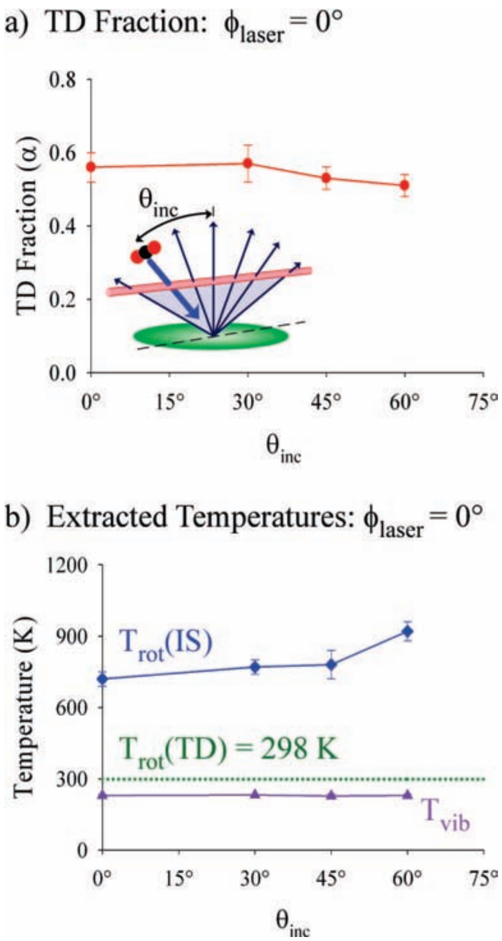

Figure 9. Extracted fit parameters from a two-temperature analysis of scattered CO_2 populations detected in the $\varphi_{laser} = 0°$ configuration. The TD fraction is plotted versus θ_{inc} in panel (a), while T_{rot}(TD/IS) and T_{vib} are plotted in (b).

distributions will likely involve forward-peaked "lobular" patterns, such as described by $\cos^n(\theta_{scat} - \theta')$.[32,61,62] As noted previously, for example, Minton and co-workers have observed strongly directional in-plane ($\varphi_{scat} = 0°$) patterns for scattering of O atoms from squalane $C_{30}H_{62}$ (l) at $\theta_{inc} = 60°$,[32,58] which can be reasonably well characterized by $\approx\cos^6(\theta_{scat} - 37°)$. While such an in-plane characterization ($\varphi_{scat} = 0°$) depends only on θ_{scat}, the inclusion of out-of-plane scattering events will clearly require additional modeling of the dependence on φ_{scat}. However, full characterization of out-of-plane scattering events ($\varphi_{scat} > 0°$) has long remained an ongoing experimental challenge, with very few successful examples from the molecular beam literature.[60] Though also quite challenging, direct absorption laser methods offer a powerful alternative for such 3D characterization of both in-plane and out-of-plane scattering processes, where the information is "encoded" within the high-resolution Doppler profiles for a series of laser probe geometries. Though not there yet, efforts toward obtaining a full 3D reconstruction of the quantum-state-resolved fluxes for CO_2 scattering from PFPE are currently underway.[72]

Even so, we can offer the following initial observations. The quantum-state-resolved sticking probabilities reported in our work are extracted from column densities over the length of the laser detection region and, thus, for $\varphi_{laser} = 90°$, represents integration over both in-plane and out-of-plane scattering dynamics. However, for $\varphi_{laser} = 0°$, integration over column densities samples populations that arise from predominantly in-plane scattering events. Therefore, comparison of results from $\varphi_{laser} = 0°$ versus 90° configurations may offer some insights into these two classes of scattering events. For example, populations measured in the $\varphi_{laser} = 90°$ geometry at $\theta_{inc} = 60°$ progress from predominantly TD at $\theta_{scat} = -60°$ ($\alpha \approx 0.67$) to mostly IS for $\theta_{scat} = 60°$ ($\alpha \approx 0.29$). This trend is, of course, consistent with lobular scattering in the forward direction but does not distinguish between in-plane versus out-of-plane dynamics. For in-plane scattering events sampled with the $\varphi_{laser} = 0°$ probe geometry, two-temperature fits to the populations yield nearly constant $\alpha \approx 0.5$ for $\theta_{inc} = 0°, 30°, 45°$, and 60°. At first glance, this would appear to be just the average α value for $\varphi_{laser} = 90°$ over the range of $\theta_{scat} = -60°$ to $+60°$. However, due to preferential forward scattering in the IS component noted above, flux into $\theta_{scat} > 0°$ will be weighted more than that for $\theta_{scat} < 0°$. Thus, a correctly flux-weighted average for α at $\varphi_{laser} = 90°$ will be substantially less than the above simple average over $\theta_{scat} = -60°$ to $+60°$. As a result, the data indicate a greater propensity for IS scattering when

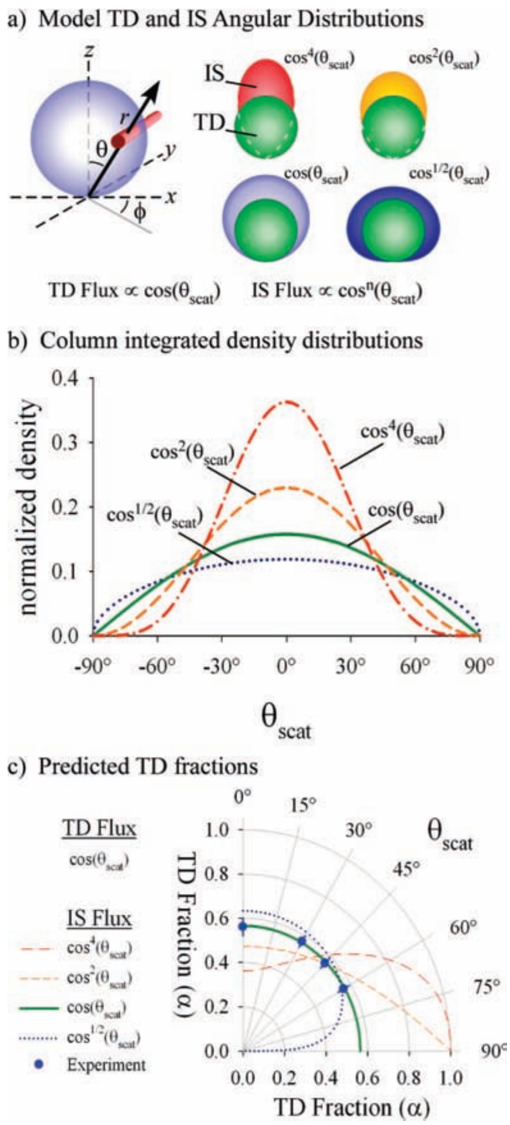

Figure 10. Model and experimental angular distributions for scattered TD and IS flux. (a) Illustrations of flux for different assumed $\cos^n(\theta_{scat})$ distributions. (b) Normalized column density as a function of scattering angle for different n values. (c) Direct comparison between experimental TD sticking probabilities for $\theta_{inc} = 0°$ and calculated values based on $F_{IS} \propto \cos^n\theta_{scat}$. The data clearly support a simple "effusive" $\cos(\theta_{scat})$ model (i.e., $n \approx 1.0 \pm 0.2$) for the IS channel under normal incidence conditions.

Doppler profiles are integrated over both in-plane and out-of-plane directions ($\varphi_{\text{laser}} = 90°$) rather than purely in-plane directions ($\varphi_{\text{laser}} = 0°$). Simply stated, this comparison reveals the importance of *out-of-plane* trajectories as CO_2 scatters via the IS versus TD channels, a prediction that can be further tested and quantified by detailed analysis of the Doppler profiles.

V. Conclusion and Summary

Experimental gas–liquid scattering experiments have probed the effects of incident molecular beam angle on the final scattering distributions. Specifically, quantum state rotational and vibrational populations of CO_2 have been measured as a function of final scattering angle for incident angles of $\theta_{\text{inc}} = 0°-60°$, sampled with laser probe geometries both parallel ($\varphi_{\text{laser}} = 0°$) and perpendicular ($\varphi_{\text{laser}} = 90°$) to the scattering plane. At all angles, the high incident collision energy ($E_{\text{inc}} = 10.6(8)$ kcal/mol) leads to two-channel scattering dynamics that reflect trapping desorption (TD) and impulsive scattering (IS). The internal state populations are well-fit at all angles by a two-temperature Boltzmann analysis that characterizes both IS and TD distributions with a rotational temperature. The trapping desorption fraction, α, and $T_{\text{rot}}(\text{IS})$ are determined as a function of final scattering angle, θ_{scat}, for conditions that include normal to grazing incidence. Additionally, vibrational energy transfer is monitored by a direct comparison of populations in the 00^00 and 01^10 vibrational states, which show sub-T_S distributions in the scattered flux.

Final recoil information is extracted for normal incidence based on a model that characterizes the flux from the IS channel as a $\cos^n(\theta_{\text{scat}})$ angular distribution. The TD fraction is used to extract the value of $n = 1.0 \pm 0.2$ based on the observation that α remains nearly constant for $\theta_{\text{scat}} = 0°-60°$. The final distribution of all molecules simply appears to be characterized by TD and IS components, which each are described by $\cos(\theta_{\text{scat}})$ patterns. Experiments for $\theta_{\text{inc}} > 0°$ illustrate deviations from $\cos^n(\theta_{\text{scat}})$ scattering distributions based on the two-channel dynamics probed for a series of experimental geometries. The IS flux appears to preferentially scatter in the forward direction based on a decreased TD fraction for the populations measured at these angles. In a correlated fashion, state populations reveal primarily TD events in the backward directions. The experimental geometries probe both in-plane and out-of-plane scattering, which are both important types of scattering trajectories in the IS channel.

Acknowledgment. Primary support for this work has been provided by the Air Force Office of Scientific Research, with additional equipment funding provided by the National Science Foundation. We would also like to take the opportunity to thank Professor Stephen R. Leone for his many brilliant contributions to the chemical physics community, as well as, on a more personal note, being an inspiring academic mentor, excellent colleague, and true personal friend.

References and Notes

(1) Leone, S. R.; Wodarczyk, F. J. *J. Chem. Phys.* **1974**, *60*, 314.

(2) Leone, S. R. *J. Phys. Chem. Ref. Data* **1982**, *11*, 953.

(3) Leone, S. R. *Annu. Rev. Phys. Chem.* **1984**, *35*, 109.

(4) Weisshaar, J. C.; Zwier, T. S.; Leone, S. R. *J. Chem. Phys.* **1981**, *75*, 4873.

(5) Zwier, T. S.; Bierbaum, V. M.; Ellison, G. B.; Leone, S. R. *J. Chem. Phys.* **1980**, *72*, 5426.

(6) Lin, K. C.; Kleiber, P. D.; Wang, J. X.; Stwalley, W. C.; Leone, S. R. *J. Chem. Phys.* **1988**, *89*, 4771.

(7) Lindner, J.; Lundberg, J. K.; Lovejoy, C. M.; Leone, S. R. *J. Chem. Phys.* **1997**, *106*, 2265.

(8) Lauenstein, C. P.; Bastian, M. J.; Bierbaum, V. M.; Penn, S. M.; Leone, S. R. *J. Chem. Phys.* **1991**, *94*, 7810.

(9) Magnotta, F.; Nesbitt, D. J.; Leone, S. R. *Chem. Phys. Lett.* **1981**, *83*, 21.

(10) Neumark, D. M.; Wodtke, A. M.; Robinson, G. N.; Hayden, C. C.; Lee, Y. T. *Phys. Rev. Lett.* **1984**, *53*, 226.

(11) Greene, C. H.; Zare, R. N. *Annu. Rev. Phys. Chem.* **1982**, *33*, 119.

(12) Simpson, W. R.; Orr Ewing, A. J.; Zare, R. N. *Chem. Phys. Lett.* **1993**, *212*, 163.

(13) Crim, F. F. *Annu. Rev. Phys. Chem.* **1993**, *44*, 397.

(14) Polanyi, J. C. *Acc. Chem. Res.* **1972**, *5*, 161.

(15) Weitz, E.; Flynn, G. *Annu. Rev. Phys. Chem.* **1974**, *25*, 275.

(16) Perkins, B. G.; Haber, T.; Nesbitt, D. J. *J. Phys. Chem. B* **2005**, *109*, 16396.

(17) Perkins, B. G.; Nesbitt, D. J. *J. Phys. Chem. B* **2006**, *110*, 17126.

(18) Perkins, B. G.; Nesbitt, D. J. *J. Phys. Chem. A* **2007**, *111*, 7420.

(19) Perkins, B. G.; Nesbitt, D. J. *J. Phys. Chem. B* **2008**, *112*, 507.

(20) Zolot, A. M.; Harper, W. W.; Perkins, B. G., Jr.; Dagdigian, P. J.; Nesbitt, D. J. *J. Chem. Phys.* **2006**, *125*, 021101.

(21) Perkins, B. G.; Nesbitt, D. J. PNAS, **2008**, 10.1073/pnas.0800401105.

(22) Jaeger, A. O. *Ind. Eng. Chem.* **1929**, *21*, 627.

(23) Williams, A. *Combust. Flame* **1973**, *21*, 1.

(24) Jimenez, J. L.; Jayne, J. T.; Shi, Q.; Kolb, C. E.; Worsnop, D. R.; Yourshaw, I.; Seinfeld, J. H.; Flagan, R. C.; Zhang, X. F.; Smith, K. A.; Morris, J. W.; Davidovits, P. *J. Geophys. Res., [Atmos.]* **2003**, 108.

(25) Ellison, G. B.; Tuck, A. F.; Vaida, V. *J. Geophys. Res., [Atmos.]* **1999**, *104*, 11633.

(26) Ramanathan, V.; Crutzen, P. J.; Kiehl, J. T.; Rosenfeld, D. *Science* **2001**, *294*, 2119.

(27) Gertner, B. J.; Hynes, J. T. *Science* **1996**, *271*, 1563.

(28) Solomon, S. *Rev. Geophys.* **1999**, *37*, 275.

(29) Solomon, S.; Garcia, R. R.; Rowland, F. S.; Wuebbles, D. J. *Nature* **1986**, *321*, 755.

(30) Saecker, M. E.; Govoni, S. T.; Kowalski, D. V.; King, M. E.; Nathanson, G. M. *Science* **1991**, *252*, 1421.

(31) Shuler, S. F.; Davis, G. M.; Morris, J. R. *J. Chem. Phys.* **2002**, *116*, 9147.

(32) Minton, T. K.; Garton, D. J. Dynamics of Atomic-Oxygen-Induced Polymer Degradation in Low Earth Orbit. In *Chemical Dynamics in Extreme Environments*; Dressler, R. A., Ed.; World Scientific Publishing Co.: Singapore, 2001; p 420.

(33) Gibson, K. D.; Isa, N.; Sibener, S. J. *J. Chem. Phys.* **2003**, *119*, 13083.

(34) Sinha, M. P.; Fenn, J. B. *5th International Symposium on Molecular Beams*; Lab Phys Mol Hautes Engeries, Peymejnade, France, 1975.

(35) Martinez-Nunez, E.; Rahaman, A.; Hase, W. L. *J. Phys. Chem. C* **2007**, *111*, 354.

(36) Isa, N.; Gibson, K. D.; Yan, T.; Hase, W.; Sibener, S. J. *J. Chem. Phys.* **2004**, *120*, 2417.

(37) Vazquez, S. A.; Morris, J. R.; Rahaman, A.; Mazyar, O. A.; Vayner, G.; Addepalli, S. V.; Hase, W. L.; Martinez-Nunez, E. *J. Phys. Chem. A* **2007**, *111*, 12785.

(38) Scott Day, B.; Morris, J. R.; Troya, D. *J. Chem. Phys.* **2005**, *122*, 214712.

(39) Day, B. S.; Morris, J. R.; Alexander, W. A.; Troya, D. *J. Phys. Chem. A* **2006**, *110*, 1319.

(40) Yan, T. Y.; Hase, W. L. *J. Phys. Chem. B* **2002**, *106*, 8029.

(41) Troya, D.; Schatz, G. C. *J. Chem. Phys.* **2004**, *120*, 7696.

(42) Tasic, U.; Day, B. S.; Yan, T.; Morris, J. R.; Hase, W. L. *J. Phys. Chem. C* **2008**, *112*, 476.

(43) Nathanson, G. M. *Annu. Rev. Phys. Chem.* **2004**, *55*, 231.

(44) Yan, T. Y.; Hase, W. L.; Barker, J. R. *Chem. Phys. Lett.* **2000**, *329*, 84.

(45) Saecker, M. E.; Nathanson, G. M. *J. Chem. Phys.* **1994**, *100*, 3999.

(46) Saecker, M. E.; Nathanson, G. M. *J. Chem. Phys.* **1993**, *99*, 7056.

(47) King, M. E.; Nathanson, G. M.; Hanninglee, M. A.; Minton, T. K. *Phys. Rev. Lett.* **1993**, *70*, 1026.

(48) King, M. E.; Fiehrer, K. M.; Nathanson, G. M.; Minton, T. K. *J. Phys. Chem. A* **1997**, *101*, 6556.

(49) Morris, J. R.; Behr, P.; Antman, M. D.; Ringeisen, B. R.; Splan, J.; Nathanson, G. M. *J. Phys. Chem. A* **2000**, *104*, 6738.

(50) Klassen, J. K.; Fiehrer, K. M.; Nathanson, G. M. *J. Phys. Chem. B* **1997**, *101*, 9098.

(51) Manning, M.; Morgan, J. A.; Castro, D. J.; Nathanson, G. M. *J. Chem. Phys.* **2003**, *119*, 12593.

(52) Cohen, S. R.; Naaman, R.; Sagiv, J. *Phys. Rev. Lett.* **1987**, *58*, 1208.

(53) Day, B. S.; Shuler, S. F.; Ducre, A.; Morris, J. R. *J. Chem. Phys.* **2003**, *119*, 8084.

(54) Cohen, S. R.; Naaman, R.; Sagiv, J. *J. Chem. Phys.* **1988**, *88*, 2757.

(55) Day, B. S.; Morris, J. R. *J. Phys. Chem. B* **2003**, *107*, 7120.

(56) Alexander, W. A.; Day, B. S.; Moore, H. J.; Lee, T. R.; Morris, J. R.; Troya, D. *J. Chem. Phys.* **2008**, 128.

(57) Day, B. S.; Davis, G. M.; Morris, J. R. *Anal. Chim. Acta* **2003**, *496*, 249.

(58) Zhang, J.; Garton, D. J.; Minton, T. K. *J. Chem. Phys.* **2002**, *117*, 6239.

(59) Garton, D. J.; Minton, T. K.; Alagia, M.; Balucani, N.; Casavecchia, P.; Volpi, G. G. *J. Chem. Phys.* **2000**, *112*, 5975.

(60) Minton, T. K.; Tagawa, M.; Nathanson, G. M. *J. Spacecr. Rockets* **2004**, *41*, 389.

(61) Lykke, K. R.; Kay, B. D. *J. Chem. Phys.* **1990**, *92*, 2614.

(62) Rettner, C. T.; Kimman, J.; Auerbach, D. J. *J. Chem. Phys.* **1991**, *94*, 734.

(63) Comsa, G.; David, R. *Surf. Sci. Rep.* **1985**, *5*, 145.

(64) Rettner, C. T.; Schweizer, E. K.; Mullins, C. B. *J. Chem. Phys.* **1989**, *90*, 3800.

(65) Proch, D.; Trickl, T. *Rev. Sci. Instrum.* **1989**, *60*, 713.

(66) Lednovich, S. L.; Fenn, J. B. *AIChE J.* **1977**, *23*, 454.

(67) The notation ($\nu_1\ \nu_2{}^{l}\ \nu_3$) characterizes the vibrational state of CO_2; the quantum numbers ν_1, ν_2, and ν_3 describe the symmetric stretch, bend, and antisymmetric stretch, and l is the vibrational angular momentum quantum number.

(68) Kaur, D.; Desouza, A. M.; Wanna, J.; Hammad, S. A.; Mercorelli, L.; Perry, D. S. *Appl. Opt.* **1990**, *29*, 119.

(69) Johns, J. W. C. *J. Mol. Spectrosc.* **1987**, *125*, 442.

(70) Miller, D. R. Free Jet Sources, In *Atomic and Molecular Beam Methods*; Scoles, G., Ed.; Oxford University Press: New York, 1988; Vol. 1, p 14.

(71) Nizkorodov, S. A.; Harper, W. W.; Chapman, W. B.; Blackmon, B. W.; Nesbitt, D. J. *J. Chem. Phys.* **1999**, *111*, 8404.

(72) Perkins, B. G.; Ormond, T.; Nesbitt, D. J. Work in progress.

JP8022887